RSC Advances

PAPER

View Article Online
View Journal | View Issue

Cite this: *RSC Adv.*, 2021, **11**, 7096

Ferromagnetic alloy for high-efficiency photovoltaic conversion in solar cells: first-principles insights when doping SnO_2 rutile with coupled Eu–Gd

A. Fakhim Lamrani *

From results of first-principles all-electron full-potential augmented spherical-wave calculations within a generalized gradient approximation, a materials design for half-metallic ferromagnetic semiconductors based on (Eu,Gd)-doped SnO_2 rutile is proposed. Moreover, their half-metallic ferromagnetic properties are homogenous and energetically stable for different crystallographic directions. Therefore, the interatomic exchange interaction between the spins of double impurity ions is a long-range ferromagnetic interaction that is sharply weakened when the distance between Eu–Gd increases. The double impurities most likely substitute adjacent Sn sites and result in strong ferromagnetic interactions by p–f hybridization between rare earth 4f and Op states. There is great interest in the configuration that has the lowest energy difference, where the double impurity substitutes the nearest neighbor Sn sites along the *z*-axis of SnO_2 rutile. Generalized gradient approximation GGA and GGA+U calculations were performed. According to our revPBE-GGA calculations, the ferromagnetic compound is capable of absorbing 96% from the visible light. Furthermore, the transport properties at room temperature ensure excellent electrical conductivity, low thermal conductivity, and the most optimal figure of merit (*ZT*), which leads to high thermoelectric performance. As the latter are closely related to free flow charge carriers, we can subsequently predict that the ferromagnetic alloy will be able to be a great power source for highly effective photovoltaic conversion in solar cells. Further experimentation will be necessary to obtain confirmation of our *ab initio* predictions.

Received 5th January 2021
Accepted 28th January 2021

DOI: 10.1039/d1ra00088h

rsc.li/rsc-advances

1 Introduction

Because of their many favorable attributes, oxide-based diluted magnetic semiconductors (DMS), particularly SnO_2, are highly appropriate for constructing spintronic devices compared to non-oxide-based DMS.[1] Because of the physical properties of tin oxide (SnO_2), which include excellent optical transparency, metal-like conductivity, and high chemical stability, it is a highly multifunctional material with widespread applicability. Many great developments have also occurred in condensed matter physics for the creation of innovative functions.[2,3]

Since the observation of high-temperature ferromagnetism in Co-doped SnO_2 films by Ogale *et al.*,[4] and the development of a transparent ferromagnet with a Curie temperature of 610 K in Fe-doped SnO_2,[5] a large number of experimental and theoretical investigations have been performed using tin oxide doped with alkaline earth metals, transition metals, and rare earth ions.[6–19] Although several research groups have delved into the study of spintronics coupled with optoelectronics, the field has been largely left untouched. Specifically, the production of solar cells based on ferromagnetic DMS has not yet been accomplished, and it may be a key material used in the future technology of solar cells. Indeed, ferromagnetic materials may display enhanced lifetimes of excited states due to spin-dependent transition selection rules, which have not yet been classified. For a photovoltaic energy conversion system, long lifetimes of excited states are important because they increase performance and provide the opportunity for photogenerated carriers to be collected. Currently, the main problem with photovoltaic solar cells is the conversion efficiency limitation,[20–24] which remains due to the discord between the solar incident spectrum and the spectral absorption of the cell's material.

Some methods have been improved that consist of modifying the solar spectrum by a wavelength conversion process to render highly effective photovoltaic conversion. There are promising up- and down-conversion approaches that are realized by doping host matrices with rare earth elements.[25,26]

Because of the electronic structure and susceptibility of magnetic and optical properties of doped SnO_2 to experimental conditions, it is preferable to conduct investigations utilizing

Nanomaterial and Nanotechnology Unit, E. N. S. Rabat, Energy Research Center, Faculty of Sciences, Mohammed V University in Rabat, B. P. 1014, Morocco. E-mail: fakhim@um5.ac.ma

theoretical calculations. Hence, the current study intends to examine the oxide-based semiconductor, SnO_2 rutile doped with double rare-earth impurities (two different ones), rather than the traditional single impurities, using first-principles insights. Thus, after identifying the exact substitution sites of the couple Eu/Gd in the host matrix of SnO_2 rutile, we attempted to understand the electronic, magnetic, and optical properties of (Eu,Gd)-doped SnO_2 rutile. Our objective behind this research is twofold:

A. To supply a more accurate and complementary study on the electronic structure, and to describe the magnetic ground state of $Sn_{14}EuGdO_{32}$ using first-principles calculations based on revPBE-GGA. Then, we introduce results from revPBE-GGA+U calculations.

B. To understand the rendering of this ferromagnetic DMS under natural light, which is predominantly in the visible region, and its ability to participate in photovoltaic conversion in a solar cell.

2 Theoretical method

The calculations are based on density functional theory and the generalized gradient approximation (GGA)[27] with the local density approximation parametrized according to Vosko, Wilk and Nusair (VWN).[28] They were performed using the scalar-relativistic implementation of the augmented spherical wave (ASW) method (see ref. 29–31 and references therein). With the ASW method, the wave function is expanded in atom-centered augmented spherical waves, which are Hankel functions and numerical solutions of Schrödinger's equation, respectively, outside and inside the so-called augmentation spheres. In order to optimize the basis set, additional augmented spherical waves are placed at carefully selected interstitial sites. The choice of these sites as well as the augmentation radii were automatically determined using the sphere geometry optimization algorithm.[32]

Self-consistency was achieved by a highly efficient algorithm for convergence acceleration[33] until the variation of the atomic charges was smaller than 10^{-8} electrons and the variation of the total energy was smaller than 10^{-8} Ryd. The Brillouin zone integrations were performed using the linear tetrahedron method with up to $6 \times 6 \times 9$ k-points corresponding to 324 k points within the irreducible wedge.[31,34] In the present work, we used a new full-potential version of the ASW method, which was implemented only very recently.[35] In this version, the electron density and related quantities are given by a spherical harmonics expansion inside the muffin-tin spheres. In the remaining interstitial region, a representation in terms of atom-centered Hankel functions is used.[36] However, in contrast to previous related implementations, it is unnecessary to use a so-called multiple-k basis set, and this allows for a very high computational speed of the resulting scheme.

SnO_2 possesses tetragonal symmetry in the rutile structure. The rutile structure is characterized by two lattice parameters, a = 4.7373 Å and c = 3.1864 Å.[37] The unit cell contains two metal atoms (Sn) at positions (0, 0, 0) and (1/2, 1/2, 1/2) and four oxygen atoms (O) at positions $\pm$ (u, u, 0; 1/2 + u, 1/2 − u, 1/2) with u = 0.306. Each Sn atom is in the central site of an octahedron, which is formed by four rectangular basal O atoms (O_1) and two vertex O atoms (O_2). Using the integer multiple representations of the primitive lattice vectors a, b, and c of the conventional SnO_2 cell, the geometry of an undoped $2 \times 2 \times 2$ supercell containing 48 atoms ($Sn_{16}O_{32}$) was determined. In order to model a composition $Sn_{1-x}Eu_xO_2$, $Sn_{1-x}Gd_xO_2$, and $Sn_{1-2x}Eu_xGd_xO_2$ for $x = 0.0625$, one and two different Sn atoms are substituted. Two possible couplings [ferromagnetic (FM) and antiferromagnetic (AFM)] have been considered, between the double impurities.

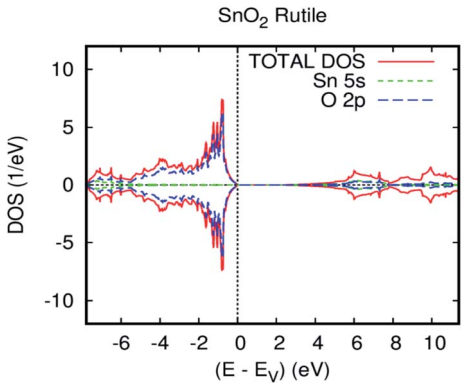

Fig. 1 The GGA total and partial DOS of SnO_2 rutile.

3 Results and discussion

3.1 Electronic properties

First, we confirmed the electronic structure of the parent material without any doping elements. Fig. 1 displays the revPBE-GGA total and partial density of states (DOS). The overall band structure of the present full-potential augmented spherical wave (FPASW) result is consistent with the existing results.[38,39] It can be viewed that the majority-spin and minority-spin are symmetrical, which signifies that the tin oxide rutile is a nonmagnetic material. Indeed, the valence band is chiefly dominated by O-2p orbitals and is full, whereas the conduction band is principally formed by Sn-5s and is empty.

As usual in the GGA calculations, the obtained energy gap of 2.4 eV is underestimated. In fact, this shortcoming is well known, and compensation is applied by employing the GGA.[40] In particular, we find a valence band width of 7.7 eV in accordance with the experimental data (7.5 eV mentioned in ref. 41) and the preceding first-principles technique (7.9 eV and 8.8 eV mentioned in ref. 42). The optimized bulk cell parameters for pure SnO_2 with FPASW-GGA[43] are in accordance with experimental values[37,44] and other theoretical values.[45] This clearly illustrates that our calculation is similar to the experimental ones. A strong correlation was applied to Op-electrons (U_O = 6.25 eV), and Fig. 2 pragmatically illustrates the GGA+U calculation of the band structure of SnO_2 rutile. As a matter of fact, the GGA+U method satisfactorily[46] enhances the energy gap in comparison with revPBE-GGA (3.6 vs. 2.4 eV), and provides stronger agreement with the experimental data.[47] Additionally, the application of the Hubbard coefficient to the anion p states has a great impact on the correction of the gap energy.

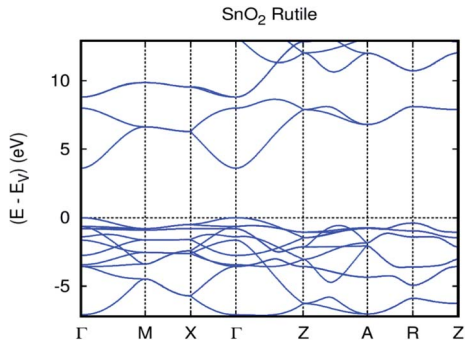

Fig. 2 The GGA+U band structure of SnO_2 rutile.

3.2 Electronic and magnetic properties

Prior to discussing the half-metallic ferromagnetic properties and high effectiveness of the photovoltaic conversion of SnO_2 rutile doped with the couple Eu/Gd, we initially examined the electronic structure and the magnetic properties of SnO_2 rutile doped with simple rare earth. Fig. 3(a) and (b) show the revPBE-GGA, the projected local DOS (PLDOS) for $Sn_{0.9375}Eu_{0.0625}O_2$, and those for $Sn_{0.9375}Gdo_{0.0625}O_2$. However, the PLDOS reveal that the europium impurity in the SnO_2 matrix is a magnetic semiconductor. On the other side, we obtained a half-metallic magnet for Gd-doped SnO_2 rutile. From Fig. 3(a), three groups of energy levels for Eu 4f in the spin-up states can be observed and partially filled. One exists at the valence band edge, the second is at the limit of the Fermi level, and the third one is above the Fermi level and is completely empty, while the spin-down-induced states, which are at the minimum of the conduction band, are completely empty. Therefore, the occupied electronic configuration of Eu-4f in $Sn_{0.9375}Eu_{0.0625}O_2$ is f^5, as presented in Table 1, and it is justifiable according to the analysis of the local magnetic moments of the impurities and the oxidation states from the charge carrier's occupancy in the 4f orbital. In contrast, it is clear from Fig. 3(b) that the Gd-based system is half-metallic [*i.e.*, for spin-up, states are available, whereas for spin-down, they are not available at the Fermi level]. A careful analysis of PLDOS indicates that the majority spin channel of Gd-4f is located at the top of the valence band and overlaps with O-2p orbitals at the Fermi level E_f. Table 1 shows that the main part of the total magnetic moment comes from the gadolinium atom, which suggests that the Gd impurity doped in SnO_2 has a magnetic configuration of $4f^6$.

To more precisely study the electronic structure and to describe the magnetic ground state of the couple europium–gadolinium-doped tin dioxide, we have: $Sn_{1-2x}Eu_xGd_xO_2$ ($x = 0.0625$). In fact, we performed the revPBE-GGA calculation for modeling the effect of interatomic exchange interactions *via* following a simple model that consists of altering the distances between double rare earth ions in the supercell. Furthermore, three separations were realized, by the fixed Eu ion at the origin of the supercell, [000], and the other ion (Gd) moving along different crystal directions. The 3.2 Å corresponds to a double impurity substitution of the nearest neighbour Sn sites along the *z*-axis of SnO_2 rutile, which indicates that Gd is placed at the site of [001], while 5.7 and 7.42 Å corresponds to farther Eu–Gd separations with Eu–O–Sn–O–Gd configurations along the plane [011], and diagonal direction [111], respectively (Table 2).

For each Eu–Gd separation, ferromagnetic (fero) and ferrimagnetic (feri) alignments of rare earth spins were considered. The total energy difference ΔE; ($\Delta E = E^{feri} - E^{fero}$) between these two alignments is a measure of interatomic exchange interaction. In Fig. 4, we plotted the energy difference between ferromagnetic and ferrimagnetic configurations *vs.* Eu–Gd distance in the unit cell for $Sn_{0.875}Euo_{0.065}Gdo_{0.065}O_2$. Ferromagnetic interaction between rare earth spins is favoured for all distance, and therefore, the exchange interaction between double impurity ions is a long-range ferromagnetic interaction, and it is weakened as the distance between Eu–Gd increases. Hence, the half-metallic ferromagnetic properties are homogenous in different crystallographic directions. As a matter of fact, the first nearest neighbour exchange interaction in the bonding direction Eu[000] → Gd[001] is the strongest, as shown in Fig. 4, where ΔE decreases sharply with d_{Eu-Gd}. This suggests that the rare earth impurities might cluster together during sample growth, rather than distribute themselves evenly over the lattice.

For the farther Eu–Gd separation of 5.7 Å, where there is no O-2p atom between europium and gadolinium, this corresponds to the Eu–O–Sn–O–Gd configuration along the plane

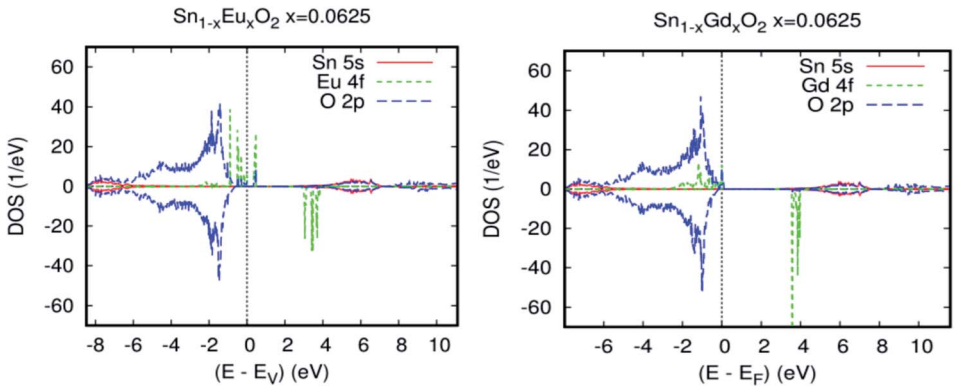

Fig. 3 (a) Projected local DOS for $Sn_{0.9375}Eu_{0.0625}O_2$, (b) Projected local DOS for $Sn_{0.9375}Gd_{0.0625}O_2$. Fermi level is set at zero.

Table 1 Total energy E_t, energy gap E_g, moment total m_t and partial m_O, and $m_{RE\ 4f}$ for SnO_2 rutile doped with simple and double rare earth

	$Sn_{0.9375}Eu_{0.0625}O_2$	$Sn_{0.9375}Gd_{0.0625}O_2$	$Sn_{0.875}Eu_{0.0625}Gd_{0.0625}O_2$	$Sn_{0.875}Eu_{0.0625}Gd_{0.0625}O_2$	$Sn_{0.875}Eu_{0.0625}Gd_{0.0625}O_2$
Compounds	GGA	GGA	GGA	GGA+U_O	GGA+$U_{O,Eu,\ and\ Gd}$
m_{4f} (μ_B)	5.2	6.14	$m_{Eu} = 5.14$; $m_{Gd} = 6.31$	$m_{Eu} = 5.2$; $m_{Gd} = 6.34$	$m_{Eu} = 5$; $m_{Gd} = 6.8$
m_O (μ_B)	−0.034	−0.042	−0.11	−0.12	0.23
m_t (μ_B)	5	6	11	11	13
E_g (eV)	0.33	2.54	2.65 (Γ to Γ)	3.85 (Γ to Γ)	1.65 (Γ to X)
E_t (Ryd)	−211836.148134	−212690.544629	222024.823722	222016.089220	222015.833623

[011]. The coupling between spins of double rare earth impurity ions is still important in comparison with that mentioned in Co- and Fe-doped SnO_2 rutile.[48] In addition, for the [111] direction, the coupling sharply decreases because the Eu–Gd separation is farther and is not communicated by the O-2p diagonal direction. Fig. 5(a) and (b) show the total and partial density of states, respectively, calculated by revPBE-GGA, for an Eu–Gd separation of 3.2 Å. The occupied electronic configuration and PLDOS of the 4f orbital in the unit cell for $Sn_{0.875}Eu_{0.065}Gd_{0.065}O_2$ appear very similar to those of the single rare earth-doped cases illustrated in Fig. 3(a) and (b). This explains that the kinetic energy gain through the hopping of spin-polarized carriers between Eu and Gd ions does not appear to occur as long as there is no sign of charge transfer between Eu and Gd. Therefore, the double-exchange mechanism will not be effective in $Sn_{1-2x}Eu_xGd_xO_2$.

On the basis of these data, we can explicate the robust ferromagnetism in the [001] and [011] directions by the p–f exchange mechanism, which weakens along the [011] plane. On the other side, the exchange interaction between spins of double rare earth in the Eu[000] → Gd[111] diagonal direction cannot be mediated by p–f hybridization because the value of ΔE is smaller in comparison with the other cases. Additionally, this study allows us to identify the exact substitution sites of the double rare earth impurities, Eu and Gd ions, in the SnO_2 matrix. It was found that the lowest difference energy corresponded to the case where the couple Eu/Gd substituted the nearest neighbor Sn sites along the *z*-axis of the unit cell $Sn_{0.875}Eu_{0.065}Gd_{0.065}O_2$. Therefore, these two rare earth impurities are likely to be located at adjacent Sn sites, and these also interact through bridging O atoms, resulting in the p–f hybridization between the rare earth 4f and Op states.

Table 2 The ferromagnetic and ferrimagnetic energy, the energy gap E_g, and partial m_O, $m_{RE\ 4f}$ *vs.* Eu–Gd distance in the unit cell for $Sn_{0.875}Euo_{0.065}Gdo_{0.065}O_2$

	d_{Eu-Gd} = 3.2 Å	d_{Eu-Gd} = 5.7 Å	d_{Eu-Gd} = 7.42 Å
d_{Eu-Gd} (Å)	Eu[000] → Gd[001]	Eu[000] → Gd[011]	Eu[000] → Gd[111]
E_{Fero} (Ryd)	−222024.828722	−222025.416400	−222024.056243
E_{Feri} (Ryd)	−222024.801777	−222025.407732	−222024.055023
E_g direct (eV)	2.65	2.764	2.81
m_{Eu} (μ_B)	5.14	5.153	5.15
m_{Gd} (μ_B)	6.31	6.221	6.20
m_0 (μ_B)	−0.11	−0.067	−0.053

Although this configuration has the lowest energy difference, in order to apply the Hubbard coefficient on the anion p states for reproducing the experimental band gap (3.60 eV) of the host system and treat the strongly correlated 4f electrons of double rare-earth impurities, the GGA+U approach was employed in addition to the generalized gradient approximation (GGA).[46] The parameter used for the O-2p state is U_O = 6.25 eV. Because both gadolinium and europium have a rather similar $4f^7$, the values of U and *J* that reproduced the experimental observation of the splitting and which we used in our calculations are 7.62 and 0.68 eV, respectively.[49] In addition, double-counting corrections were included within the fully localized limit (FLL).[46,50]

The spin density distribution for $Sn_{1-2x}Eu_xGd_xO_2$, calculated by GGA+U (U is applied only on the anion p states of the host system), is very similar to that obtained by GGA, and therefore, there is an overall topological resemblance for both methods. The signature of a half-metallic solution is clear from the PLDOS presented in Fig. 6(a). The effect of the Hubbard parameter is clear in the energy gap, as shown in Table 1. Additionally, the 4f orbitals are slightly far from the top of the valence. Thus, both majority- and minority-spins of the coupled europium–gadolinium display a band gap, which indicates that the introduction of rare earth impurities does not destroy the semiconducting nature of the parent material.

In the case where we simultaneously applied the Hubbard coefficient to the anion p states and 4f electrons, surprisingly, (Eu,Gd)-doped SnO_2 rutile displays a half-metallic characteristic

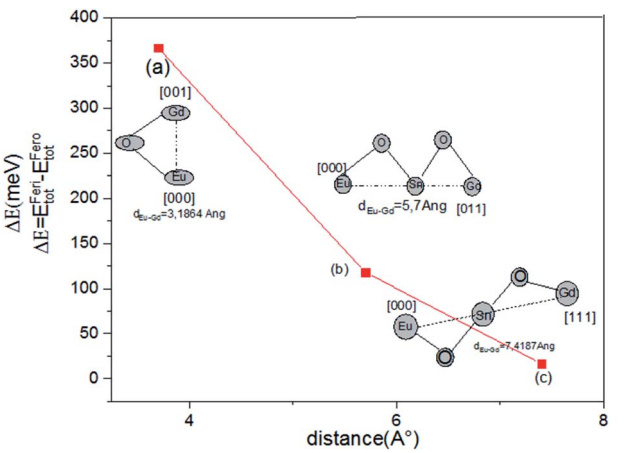

Fig. 4 The energy difference between ferromagnetic and ferrimagnetic configurations *vs.* Eu–Gd distance in the unit cell for $Sn_{0.875}Eu_{0.065}Gd_{0.065}O_2$.

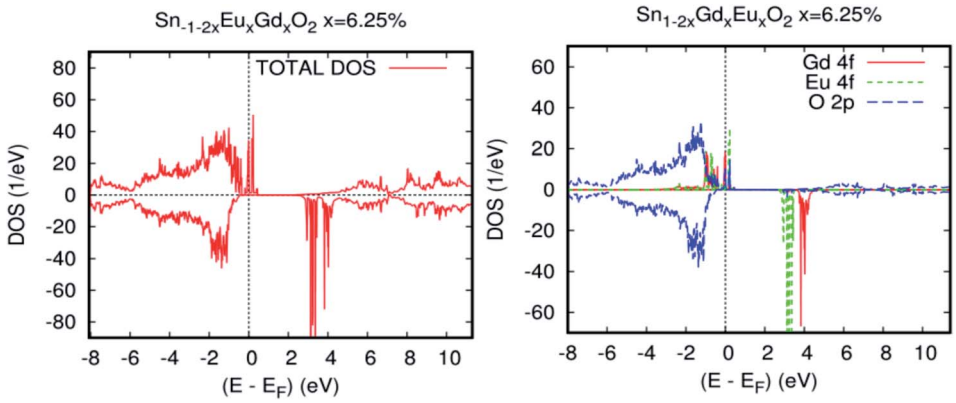

Fig. 5 Calculated spin-resolved density of states (DOS) for $Sn_{0.9375}Eu_{0.0625}Gd_{0.0625}O_2$, for an Eu–Gd separation of 3.24 Å. (a) The total DOS, and (b) the partial DOS of neighbouring Sn-5s, O-2p, and RE-4f states. The Fermi level is set at zero.

behavior, but the spin-down from the anion O-2p states is polarized at Fermi level. Indeed, the semiconducting nature has been achieved by spin-up states of Eu-4f, as shown in Fig. 6(b). Hence, the 4f states are not available at the Fermi level, and the exchange splitting increases with the increase in the atomic number of rare earth elements. It was observed that the total magnetic moment of the system became large, with 13 Bohr magnetons, μ_B, instead of 11 μ_B, for previous cases (see Table 1).

3.3 Optical properties

In this section, we examine the fundamental relationship between optical performance, electronic structure, and transport properties in order to better understand the highly effective photovoltaic conversion of SnO_2 rutile doped with double rare earth impurities (two different ones). First, we conducted a study on the optical absorption, transmissivity, reflectivity, and dielectric function of undoped SnO_2 rutile, as indicated in Fig. 7(a) and (b). The optical properties of the present FPASW on SnO_2 rutile without doped elements altogether are in conformity with the experimental and theoretical data.[51–53]

Fig. 7(a) shows the optical transmissivity, absorption, and reflectivity of pure SnO_2. It is clear that the value of transmissivity in the visible light that we have found is in the range of 89–93%, with the parent material exhibiting no response to visible light. The optical absorption coefficient is correctly defined by the rule $1 = R + A + T$, where R, A, and T denote the optical reflectivity, optical absorption coefficient, and optical transmission coefficient, respectively. To analyze the optical properties in greater detail, we require a dielectric function: $\varepsilon(\omega) = \varepsilon_1(\omega) + i\varepsilon_2(\omega)$. The imaginary part $\varepsilon_2(\omega)$ can be directly calculated from the full many-electron wave function. The real part $\varepsilon_1(\omega)$ can be determined *via* a Kramers–Kronig transform. All the other optical constants will be deduced from $\varepsilon_2(\omega)$ and $\varepsilon_1(\omega)$, such as reflectivity $R(\omega)$ and absorption coefficient $\alpha(\omega)$.[54–56]

$$\varepsilon_1(\omega) = 1 + \frac{2e}{\varepsilon_0 m^2} \sum_{VC} \int_{BZ} \frac{2dK}{(2\pi)^2} \frac{|a\ M_{CV}(K)|^2}{[E_C(K) - E_V(K)]} \frac{\hbar^3}{[E_C(K) - E_V(K)]^2 - \hbar^2\omega^2}$$

$$\varepsilon_2(\omega) = \frac{\pi}{\varepsilon_0}\left(\frac{e}{m\omega}\right)^2 \sum_{VC} \left\{ \int_{BZ} \frac{2dK}{(2\pi)^2} |aM_{CV}(K)|^2 \delta[E_C(K) - E_V(K) - \hbar\omega] \right\} \quad (2)$$

$$R(\omega) = \left|\sqrt{\varepsilon_1(\omega) + i\varepsilon_2(\omega)} - 1\right|^2 \Big/ \left|\sqrt{\varepsilon_1(\omega) + i\varepsilon_2(\omega)} + 1\right|^2 \quad (3)$$

$$\alpha(\omega) = \sqrt{2}\left[\sqrt{\varepsilon_1^2(\omega) + \varepsilon_2^2(\omega)} - \varepsilon_1(\omega)\right]^{1/2} \quad (4)$$

The subscripts C and V indicate the conduction band and the valence band, respectively. BZ denotes the first Brillouin zone, $|aM_{CV}(K)|^2$ denotes the matrix element of momentum transition, K denotes the wave vector of the first Brillouin zone, $\hbar$ denotes Planck's constant, and ω denotes the angular frequency. $E_C(K)$ and $E_V(K)$ are the intrinsic energy levels on the conduction band and the valence band, respectively.

The real and imaginary part of the dielectric function $\varepsilon = \varepsilon_1 + i\varepsilon_2$ *vs.* photon energy $h\nu$ = 0–25 eV is plotted in Fig. 7(b). The imaginary part ε_2 curve is zero below the onset of direct interband transitions between occupied and unoccupied states, and it begins to increase from $h\nu$ > 3.23 eV. The SnO_2 rutile is a transparent conductive oxide (TCO) that can be used as a transparent electrode for optoelectronic applications such as flat-screen displays, photovoltaic solar panels, or more generally, any device requiring electrical contact that does not reduce the passage of photons from the visible domain.

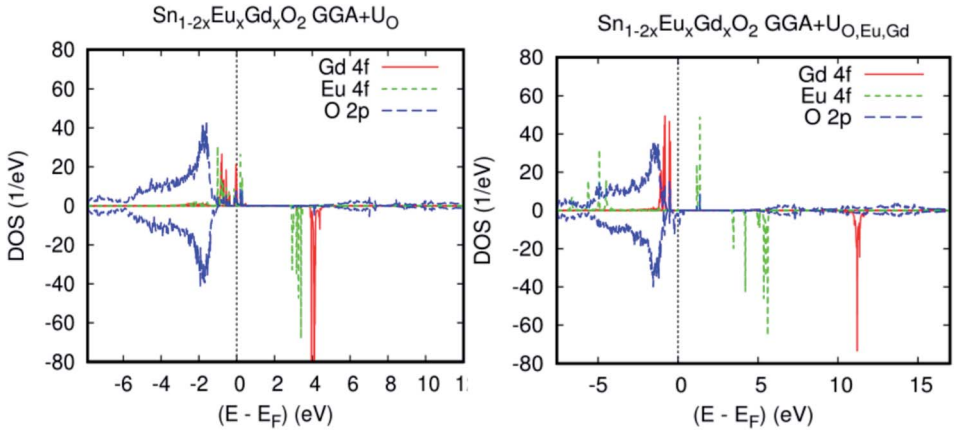

Fig. 6 The GGA+U PLDOSs of $Sn_{0.9375}Eu_{0.0625}Gd_{0.0625}O_2$ for an Eu–Gd separation of 3.24 Å. (a) The Hubbard coefficient was applied only to the anion p states of a host system. (b) The Hubbard coefficient was simultaneously applied to the anion p states and 4f electrons.

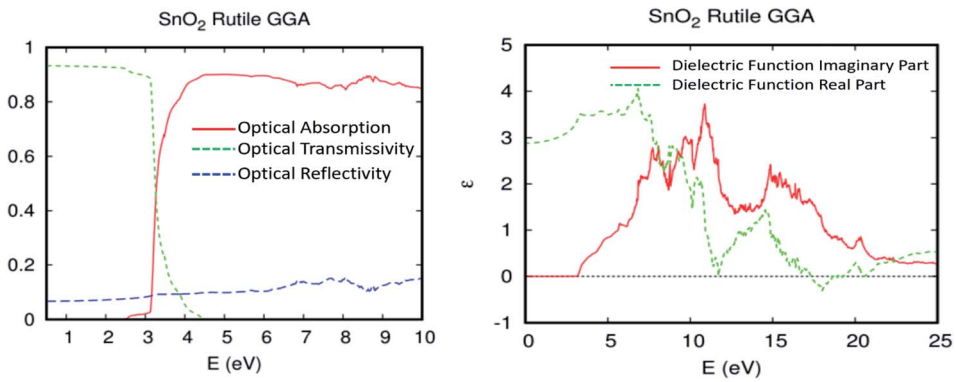

Fig. 7 (a) The optical absorption, transmissivity, and reflectivity, and (b) the real and imaginary parts of the dielectric function for SnO_2 rutile.

The insertion of coupled Eu/Gd by substitution in the SnO_2 matrix completely changes the optical properties of the parent material. The $Sn_{1-2x}Eu_xGd_xO_2$ ($x = 0.0625$) becomes a ferromagnetic alloy able to absorb maximum visible light. Fig. 8(a) depicts a plot of the predicted optical absorption, transmissivity, and reflectivity *vs.* photon energy $h\nu = 1.55$–3.2 eV of the unit cell $Sn_{0.875}Gd_{0.0625}Eu_{0.0625}O_{32}$. The thickness of the slab is fixed at $d = 1000$ nm. It seems clear that the insertion of Eu/Gd in the host system has a strong influence on the optical behavior. Therefore, we have reported a high absorption under natural light.

To put it clearly, the $Sn_{1-2x}Eu_xGd_xO_2$ ($x = 0.0625$) absorbed in the range of 83–96% of solar photons. In other words, we have a good correspondence between the incident solar spectrum and the band gap. The highly effective photonic conversion prompted us to conjecture what the two main mechanisms could be that are responsible for this yield. Consequently, the coupling of rare earth elements (two different ones) allowed us

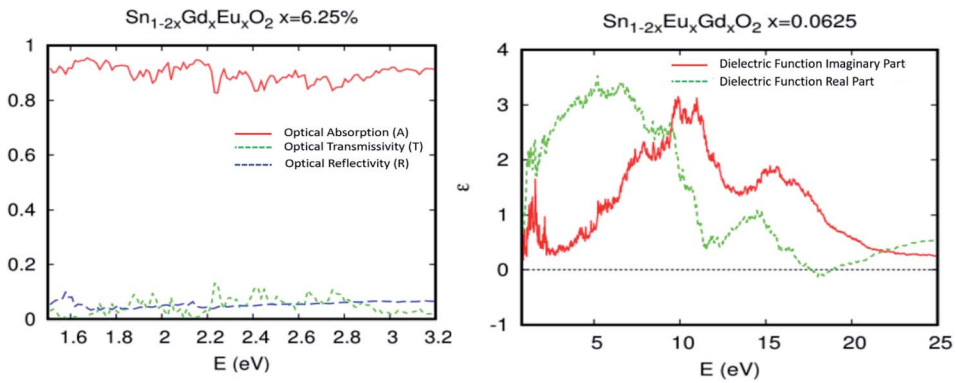

Fig. 8 (a) The optical absorption, transmissivity, and reflectivity in visible light for $Sn_{1-2x}Gd_xEu_xO_2$ $x = 0.0625$, with a fixed slab thickness of $d =$ 1000 nm. (b) The real and imaginary part of the dielectric function *versus* energy for $Sn_{1-2x}Gd_xEu_xO_2$ $x = 0.0625$.

to convert more than visible domain photons. Also, up-conversion and down-conversion have been achieved. Within this framework of down-conversion, we have found that this DSM based on the double rare earth can also absorb in the ultraviolet (UV) light region in the range of 80–92%. In fact, the high absorption of UV photons leads to a very efficient photonic conversion process, and thus, quantum cutting is occurring.

The dielectric functions presented in Fig. 8(b), which describe the absorption of electromagnetic waves attributable to interband transitions, are presented as a curve with sharper peaks in the region of lower energy photons and the photons associated with the visible domain. It should be noted that in the case of the parent material, the curve is zero in this area. This is attributed to the difference in density of states between the undoped and codoped systems, and also to the competitive role of the 4f states associated with Eu/Gd. As a consequence, the 4f states could be an effective link of free flow charge carriers between the valence band edge and the bottom of the conduction band.

For additional clarification on the advantage of SnO_2 rutile doped with double rare earth elements (two different ones) rather than the traditional single rare earth element, we have collected the optical absorption curves in the visible light region for SnO_2, $Sn_{0.875}Eu_{0.125}O_2$, $Sn_{0.875}Gd_{0.125}O_2$, and $Sn_{0.875}Gd_{0.0625}Eu_{0.0625}O_2$. The slab thickness is always fixed at d = 1000 nm. As illustrated in Fig. 9(a), the double rare earth impurities in the host matrix significantly increase the absorption in comparison with the traditional single impurity. This is attributed to the fact that quantum cutting is effective in the case of tin oxide doped with two different species of rare earth. Yet, the parent material does not absorb in the visible range.

In general, the single or double insertion of rare earth species inside a hot matrix allows quantum cutting of high-energy photons.[57–59] Moreover, for the photon conversion process to be efficient, it requires high absorption of UV photons, which is the case for the coupled Eu–Gd that would appear to be more promising in the hot matrix of SnO_2 rutile. Already, this couple has shown great power when inserted into a $LiGdF_4$ matrix.[60] Furthermore, Fig. 9(b) describes how the optical absorption, transmissivity, and reflectivity of $Sn_{14}GdEuO_{32}$ in visible light can be different depending on crystallographic directions. As an effect, the absorption study states that both A_{xx} and A_{zz} are almost optically isotropic. Therefore, the absorption underneath natural light, which is predominantly in the visible region, is uniform in all orientations. Thus, releasing electrons by the absorption of natural light is highly desirable to gain high power photovoltaic conversion, but it is insufficient.

For this reason, it is necessary to know how well $Sn_{0.875}Eu_{0.0625}Gd_{0.0625}O_2$ can allow the electric current to pass and conduct. Hence, the necessity of transport properties and the thermoelectric efficiency (η), which hinges on the thermoelectric figure of merit (zT) expressed as $zT = \frac{S^2\sigma}{k_{ele} + k_{lat}}$, where S, σ, k_{ele}, k_{lat} and T denote Seebeck coefficients, electrical conductivity, electronic thermal conductivity, lattice thermal conductivity, and temperature, respectively.[61,62]

Fig. 10(a)–(d) exhibits a plot of transport properties as a function of doping for different temperatures. The inverse relaxation time is modeled as a linear function of temperature, and correspondingly, a zeroth and a first-order term can be specified: $\frac{1}{\tau} = a_0 + a_1 T$. This leads to the correct behavior of the electrical and thermal conductivity of the common metals. The electrical conductivity, σ of $Sn_{1-2x}Eu_xGd_xO_2$, x = 0.0625%, is depicted in Fig. 10(a) and ensures excellent conductivity for this material. At room temperature, the σ value is nearly 10^5 $(\Omega\ m)^{-1}$, which corresponds to a charge carrier mobility that is sufficiently high, and the dilute ferromagnetic alloy is in the range of conductors.

We also note that the value of σ between 50 and 150 K weakly increases with increasing doping. Also, the curves associated with different doping exhibit the same behavior in the temperature range between 200 to 800 K. However, $\rho(T)$ of $Sn_{0.875}Eu_{0.0625}Gd_{0.0625}O_2$ given in Fig. 10(b) shows metal-like behavior with $\rho 300K = 2.3 \times 10^{-4}$ Ω m. An examination of the curves reveals a low electrical resistivity for all dopings, and two regimes were observed as well: transitional for $T \leq 400$ K; $\frac{d\rho}{dt} > 0$, and permanent above T_{400K}; $\frac{d\rho}{dt} = 0$. In this context, and to confirm that the heat energy was converted into electricity, the temperature dependence of the figure of merit zT as

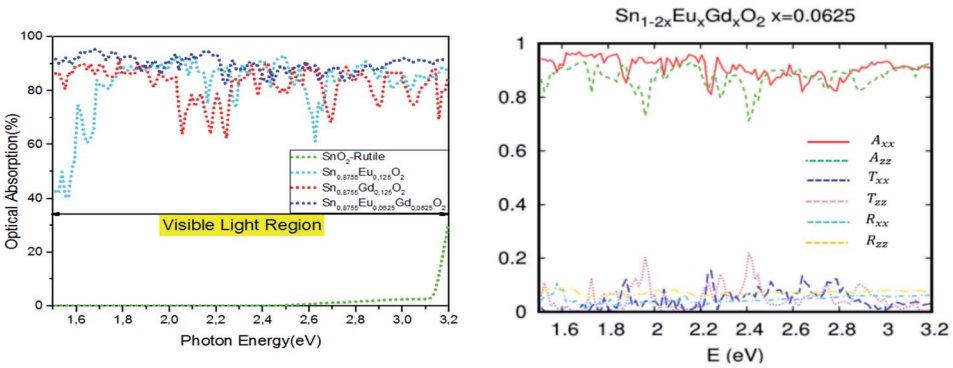

Fig. 9 The (a) optical absorption in visible light for SnO_2, $Sn_{0.875}Eu_{0.125}O_2$, $Sn_{0.875}Gd_{0.125}O_2$, and $Sn_{0.125}Eu_{0.0625}Gd_{0.0625}O_2$, with a fixed slab thickness of d = 1000 nm. (b) Optical absorption, transmissivity, and reflectivity in different crystallographic directions for $Sn_{0.9375}Eu_{0.0625}Gd_{0.0625}O_2$, with a fixed slab thickness of d = 1000 nm.

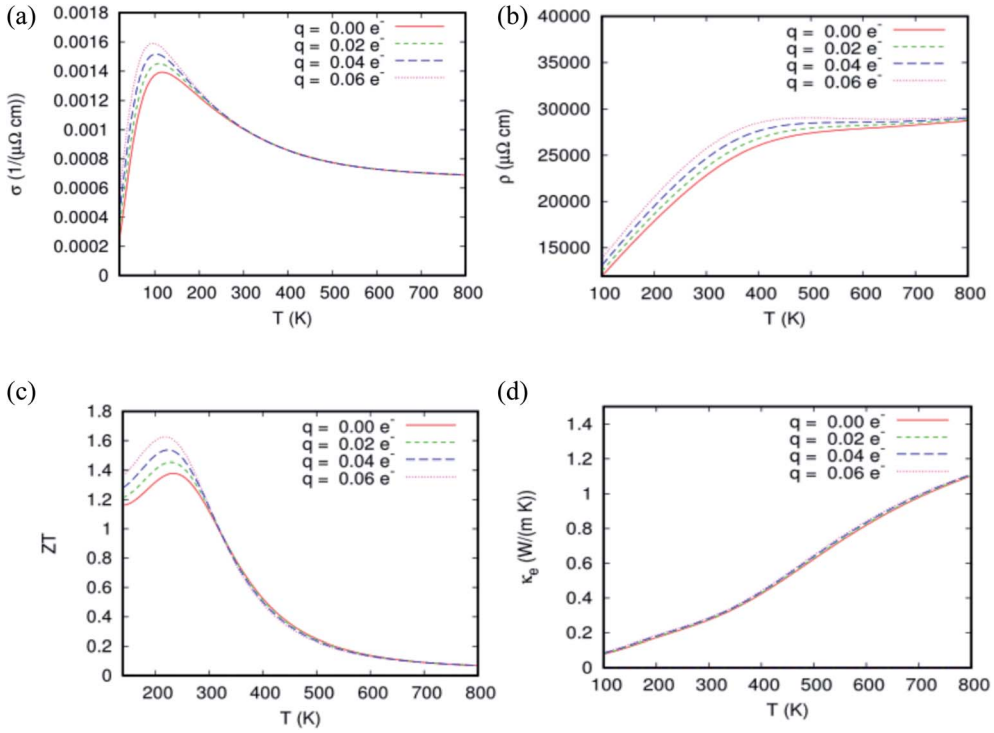

Fig. 10 (a–d) A plot of transport properties for $Sn_{0.875}Eu_{0.065}Gd_{0.065}O_2$ as a function of doping for different temperatures. (a) Electrical conductivity, (b) electrical resistivity, (c) figure of merit (*ZT*), and (d) thermal electrical conductivity.

a function of doping is plotted in Fig. 10(c). The value of zT weakly increases with increased carrier concentration in the temperature range of 100–300 K. From $T > 300$ K, the curves of the dimensionless figure of merit associated with different doping exhibit the same behavior at any given temperature. In the case of zero electrons, zT of the matrix reaches the peak (approximately 1.4) at 235 K and then begins to decrease to reach a value of 1.2 at 300 K.

The most optimal zT achieved at room temperature ensures that the material is capable of efficiently converting heat energy into electricity. Therefore, this promising thermoelectric performance is attributed to the reduction of thermal electrical conductivity by co-doping SnO_2 rutile with double rare earth. From Fig. 10(d), the κ_e of $Sn_{0.875}Eu_{0.0625}Gd_{0.0625}O_2$ compound increases with an increase in temperature. Yet, it always remains weak, and its value at $T = 300$ K is 0.3 W m^{-1} K^{-1}. Indeed, the combination of all these aspects such as the highest absorption under natural light, and the highest thermoelectric figure of merit (zT) in SnO_2 rutile doped with the coupled Eu/Gd allows us to predict that the material will be powerful and highly effective at photovoltaic conversion in solar cells, and may be a key material for the future development of solar cell technology.

Turning now to explore the pragmatic revPBE+U approach for optical absorption in the range of 400–800 nm, we have also employed the double-counting corrections included within the

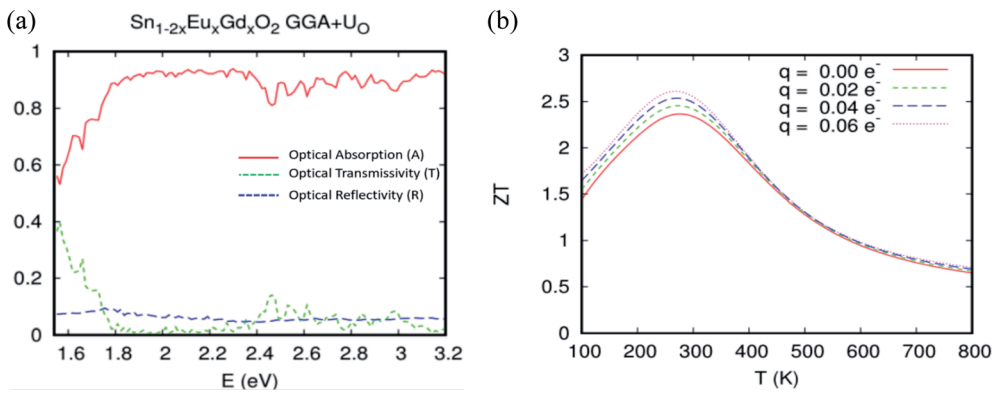

Fig. 11 The GGA+U calculation for $Sn_{0.9375}Eu_{0.0625}Gd_{0.0625}$ O_2 with the Hubbard coefficient applied only for the anion p states of the host system for a Eu–Gd separation of 3.24 Å. (a) Optical absorption, transmissivity, and reflectivity. (b) Figure of merit (*ZT*), as a function of doping for different temperatures.

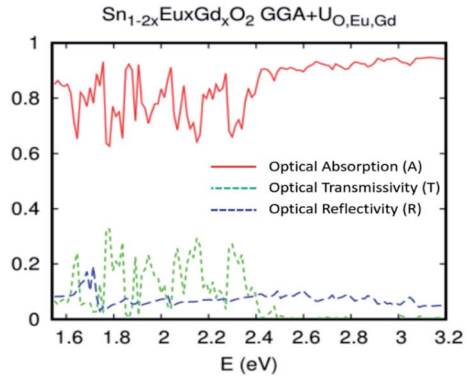

Fig. 12 The GGA+U calculation for optical absorption, transmissivity, and reflectivity of $Sn_{0.9375}Eu_{0.0625}Gd_{0.0625}O_2$, for a Eu–Gd separation of 3.24 Å. The Hubbard coefficient is simultaneously applied to the anion p states and 4f electrons.

fully localized limit. In the case where we applied the Hubbard coefficient only to the anion p states of the host system, the single-shot revPBE-GGA+U_O functional raises the gap value to 3.85 eV with an indication of a direct large half-metallic gap (Gama to Gama). As illustrated in Fig. 11(a), the optical absorption curve increases from 55% at low photon energies ($h\nu$ = 1.55 eV) to 88% at 1.79 eV from $h\nu$ > 1.72 eV. The curve behaves like the one achieved by the revPBE-GGA functional, which is a remarkable improvement in thermoelectric efficiency compared to that obtained by GGA, as illustrated in Fig. 11(b). The zT value at room temperature is 2.34 for zero carrier concentration.

The single-shot revPBE-GGA+$U_{O,Eu,Gd}$ functional reduces the gap value at 1.65 eV with an indication of a quasi-direct Γ to X band gap: the minimum that excited at Γ and X is almost the same. The optical absorption curve indicated in Fig. 12 fluctuates between 64% and 92% in the interval photon energies $h\nu$ = 1.55–2.4 eV. However, the strong absorption started from $h\nu$ > 2.4 eV and reached 92%. In a nutshell, and as expected for the competitive role of the coupled Eu/Gd in the SnO_2 host matrix, the optical absorption analysis by the different approaches used in this study roughly converge towards excellent absorption of the ferromagnetic alloy underneath natural light.

4 Conclusions

In this article, we systematically investigated the electronic structure, magnetic ground state, and optical properties of SnO_2 rutile doped with double rare earth elements (two different ones) by using DFT calculations within the GGA and GGA+U method. Therefore, the rare earth couple of europium–gadolinium is most likely located at adjacent Sn sites. The half-metallic behavior of $Sn_{0.875}Eu_{0.0625}Gd_{0.0625}O_2$ is homogenous and energetically stable for different crystallographic directions.

The results also indicate that the dilute ferromagnetic alloy is capable of absorbing up to approximately 96% in the visible light region and can efficiently convert heat energy into electricity at ambient temperature. The combination of these aspects of SnO_2 rutile doped with the couple Eu/Gd are very important for fabricating spintronic devices operating in the wavelength range of 400–800 nm that will be able to be a great source of power for high-efficiency photovoltaic conversion in solar cells.

Conflicts of interest

There are no conflicts to declare.

Acknowledgements

I would like to warmly thank Prof. Volker Eyert for the fruitful discussion concerning the transport properties implemented in the most recent version of the full potential ASW code.

References

1 T. Fukumura, Y. Yamada, H. Toyosaki, T. Hasegawa, H. Koinuma and M. Kawasaki, Exploration of oxide-based diluted magnetic semiconductors toward transparent spintronic, *Appl. Surf. Sci.*, 2004, **223**, 62–67.
2 S.-j. Zhang, C.-w. Zhang, S.-f. Zhang, W.-x. Ji, P. Li, P.-j. Wang, S.-s. Li and S.-s. Yan, Intrinsic Dirac half-metal and quantum anomalous Hall phase in a hexagonal metal-oxide lattice, *Phys. Rev. B*, 2017, **96**, 205433.
3 M.-h. Zhang, C.-w. Zhang, P.-j. Wang and S.-s. Li, Prediction of high-temperature Chern insulator with half-metallic edge states in asymmetry functionalized stanene, *Nanoscale*, 2018, **10**, 20226.
4 S. B. Ogale, R. J. Choudhary, J. P. Buban, S. E. Lofland, S. R. Shinde, S. N. Kale, V. N. Kulkarni, J. Higgins, C. Lanci, J. R. Simpson, N. D. Browning, S. D. Sarma, H. D. Drew, R. L. Greene and T. Venkatesan, High temperature ferromagnetism with a giant magnetic moment in transparent Co-doped $SnO_{2-\delta}$, *Phys. Rev. Lett.*, 2003, **91**(1–4), 077205.
5 J. M. D. Coey, A. P. Douvails, C. B. Fitzgerald and M. Venkatesan, Ferromagnetism in Fe-doped SnO_2 thin films, *Appl. Phys. Lett.*, 2004, **84**, 1332.
6 C.-w. Zhang and S.-s. Yan, First-principles study on ferromagnetism in Mg-doped SnO_2, *Appl. Phys. Lett.*, 2009, **95**, 232108.
7 C. B. Fitzgerald, M. Venkatesan, L. S. Dorneles, R. Gunning, P. Stamenov, J. M. D. Coey, P. A. Stampe, R. J. Kennedy, E. C. Moreira and U. S. Sias, Magnetism in dilute magnetic oxide thin films based on SnO_2, *Phys. Rev. B: Condens. Matter Mater. Phys.*, 2006, **74**, 115307.
8 A. Lussier, J. Dvorak, Y. U. Idzerda, S. B. Ogale, S. R. Shinde, R. J. Choudary and T. Venkatesan, Comparative X-ray absorption spectroscopy study of Co-doped SnO_2 and TiO_2, *J. Appl. Phys.*, 2004, **95**, 7190.
9 K. Gopinadhan, D. K. Pandya, S. C. Kashyap and S. Chaudhary, Cobalt-substituted SnO_2 thin films: A transparent ferromagnetic semiconductor, *J. Appl. Phys.*, 2006, **99**, 126106.

10 A. Punnoose, J. Hays, V. Gopal and V. Shutthanandan, Room-temperature ferromagnetism in chemically synthesized $Sn_{1-x}Co_xO_2$ powders, *Appl. Phys. Lett.*, 2004, **85**, 1559.

11 J. Hays, A. Punnoose, R. Baldner, M. H. Engelhard, J. Peloquin and K. M. Reddy, Relationship between the structural and magnetic properties of Co-doped SnO_2 nanoparticles, *Phys. Rev. B: Condens. Matter Mater. Phys.*, 2005, **72**, 075203.

12 X. F. Liu, Y. Sun and R. H. Yu, Role of oxygen vacancies in tuning magnetic properties of Co-doped SnO_2 insulating films, *J. Appl. Phys.*, 2007, **101**, 123907.

13 C. B. Fitzgerald, M. Venkatesan, A. P. Douvalis, S. Huber, J. M. D. Coey and T. Bakas, SnO_2 doped with Mn, Fe or Co: Room temperature dilute magnetic semiconductors, *J. Appl. Phys.*, 2004, **95**, 7390.

14 A. Punnoose, K. M. Reddy, J. Hays, A. Thurber and M. H. Engelhard, Magnetic gas sensing using a dilute magnetic semiconductor, *Appl. Phys. Lett.*, 2006, **89**, 112509.

15 N. H. Hong, J. Sakai, N. T. Huong, N. Poirot and A. Ruyter, Role of defects in tuning ferromagnetism in diluted magnetic oxide thin films, *Phys. Rev. B: Condens. Matter Mater. Phys.*, 2005, **72**, 045336.

16 S. K. Misra, S. I. Andronenko, K. M. Reddy, J. Hays and A. Punnoose, Magnetic resonance studies of Co^{2+} ions in nanoparticles of SnO_2 processed at different temperatures, *J. Appl. Phys.*, 2006, **99**, 08M106.

17 F. Hild, L. Eichenberger, A. Bouché, X. Devaux, M. Stoffel, H. Rinnert and M. Vergnat, Structural and photoluminescence properties of evaporated SnO_2 thin films doped with rare earths, *Energy Procedia*, 2015, **84**, 141–148.

18 A. Fakhim Lamrani, M. Belaiche, A. Benyoussef, A. ElKenz and E. H. Saidi, First-principles study of electronic structure and magnetic properties of doped SnO_2 (rutile) with single and double impurities, *J. Magn. Magn. Mater.*, 2011, **323**, 2982–2986.

19 A. F. Lamrani, M. Belaiche, A. Benyoussef and A. E. Kenz, Electronic structures and ferromagnetism of SnO_2 (rutile) doped with double-impurities: First-principles calculations, *J. Appl. Phys.*, 2014, **115**, 013910.

20 Q. Wang, C. Pan, K. Chen, S. Zou, M. Shen and X. Su, Efficient nanostructured quasi-single crystalline silicon solar cells by metal-catalyzed chemical etching, *Sol. Energy Mater. Sol. Cells*, 2017, **164**, 40–46.

21 V. Jovanov, E. Moulin, F. J. Haug, A. Tamang, S. I. H. Bali, C. Ballif and D. Knipp, From randomly self-textured substrates to highly efficient thin film solar cells: Influence of geometric interface engineering on light trapping, plasmonic losses and charge extraction, *Sol. Energy Mater. Sol. Cells*, 2017, **160**, 141–148.

22 M. A. Green, K. Emery, Y. Hishikawa, W. Warta and E. D. Dunlop, Solar cell efficiency table (Version 45), *Prog. Photovolt: Res. Appl.*, 2015, **23**, 1–9.

23 Y. Lin, D. Y. Kim, A. Lambertz and K. Ding, Post-deposition catalytic-doping of microcrystalline silicon thin layer for application in silicon heterojunction solar cell, *Thin Solid Films*, 2017, **635**, 63–65.

24 A. C. Lokhande, R. B. V. Chalapathy, M. He, E. Jo, M. Gang, S. A. Pawar, C. D. Lakhande and J. H. Kim, Development of Cu_2SnS_3 (CTS) thin film solar cells by physical techniques: A status review, *Sol. Energy Mater. Sol. Cells*, 2016, **153**, 84–107.

25 T. Trupke, M. A. Green and P. Würfel, Improving solar cell efficiencies by up-conversion of sub-band-gap light, *J. Appl. Phys.*, 2002, **92**, 4117–4122.

26 W. W. Peper, J. A. DeLuca and F. S. Ham, Cascade fluorescent decay of Pr^{3+} doped fluorides: achievement of a quantum yield greater emission than unity for emission of visible light, *J. Lumin.*, 1974, **8**, 344–348.

27 Y. Zhang and W. Yang, Comment on "Generalized Gradient Approximation Made Simple", *Phys. Rev. Lett.*, 1998, **80**, 890.

28 S. H. Vosko, L. Wilk and M. Nusair, Accurate spin-dependent electron liquid correlation energies for local spin density calculations: a critical analysis, *Can. J. Phys.*, 1980, **58**, 1200–1211.

29 A. R. Williams, J. Kübler and C. D. Gelatt Jr, Cohesive properties of metallic compounds: Augmented-spherical-wave calculations, *Phys. Rev. B: Condens. Matter Mater. Phys.*, 1979, **19**, 6094.

30 V. Eyert, Basic notions and applications of the augmented spherical wave method, *Int. J. Quantum Chem.*, 2000, **77**, 1007–1031.

31 V. Eyert, The Augmented Spherical Wave Method A Comprehensive Treatment, *Lect. Notes Phys.*, Springer, 2007, p. 719.

32 V. Eyert and K.-H. Höck, Electronic structure of V_2O_5: Role of octahedral deformations, *Phys. Rev. B: Condens. Matter Mater. Phys.*, 1998, **57**, 12727.

33 V. Eyert, A Comparative Study on Methods for Convergence Acceleration of Iterative Vector Sequences, *J. Comput. Phys.*, 1996, **124**, 271–285.

34 P. E. Blöch, O. Jepsen and O. K. Andersen, Improved tetrahedron method for Brillouin-zone integrations, *Phys. Rev. B: Condens. Matter Mater. Phys.*, 1994, **49**, 16223.

35 V. Eyert, The Augmented Spherical Wave Method – A Comprehensive Treatment, *Lect. Notes Phys.*, Springer, Berlin Heidelberg, 2nd edn, 2013, p. 849.

36 M. S. Methfessel, Elastic constants and phonon frequencies of Si calculated by a fast full-potential linear-muffin-tin-orbital method, *Phys. Rev. B: Condens. Matter Mater. Phys.*, 1988, **38**, 1537.

37 A. A. Bolzan, C. Fong, B. J. Kennedy and C. J. Howard, Structural Studies of Rutile-Type Metal Dioxides, *Acta Crystallogr., Sect. B: Struct. Sci.*, 1997, **53**, 373–380.

38 Z. Nabi, A. Kellou, S. Mecabih, A. Khalfi and N. Benosman, Opto-electronic properties of rutile SnO_2 and orthorhombic SnS and SnSe compounds, *Mater. Sci. Eng., B*, 2003, **98**, 104–115.

39 W. Z. Xiao, L. L. Wang, L. Xu, Q. Wan and B. S. Zou, Magnetic properties in Nitrogen-doped SnO_2 from first-principle study, *Solid State Commun.*, 2009, **149**, 1304–1307.

40 M. R. Dreizler and K. U. E. Gross, *Density Functional Theory An Approach to the Quantum Many Body Problem*, Springer, Berlin, 1990, DOI: 10.1007/978-3-642-86105-5.

41 J. M. Themlin, R. Sporken, J. Darville, R. Caudano, J. M. Gilles and R. L. Johnson, Resonant-photoemission study of SnO_2: Cationic origin of the defect band-gap states, *Phys. Rev. B: Condens. Matter Mater. Phys.*, 1990, **42**, 11914.

42 M. A. Maki-Jaskari and T. T. Rantala, Band structure and optical parameters of the SnO_2(110) surface, *Phys. Rev. B: Condens. Matter Mater. Phys.*, 2001, **64**, 075407.

43 A. Fakhim Lamrani, *Modélisation et Simulation par la DFT des Oxydes Magnétiques Dilués*, Editions Universitaires Européennes, Détails du Livre: ISBN-13 :978-3-330-86658-4, ISBN-10: 3330866586, EAN: 9783330866584, Publié le: 11.04.2017, Nombre de pages: 156.

44 W. H. Baur and A. A. Khan, Rutile-type compounds. IV. SiO_2, GeO_2 and a comparison with other rutile-type structures, *Acta Crystallogr., Sect. B: Struct. Crystallogr. Cryst. Chem.*, 1971, **27**, 2133–2139.

45 A. Beltran, J. Andrés, J. R. Sambrano and E. Longo, Density Functional Theory Study on the Structural and Electronic Properties of Low Index Rutile Surfaces for $TiO_2/SnO_2/TiO_2$ and $SnO_2/TiO_2/SnO_2$ Composite Systems, *J. Phys. Chem. A*, 2008, **112**(38), 8943–8952.

46 V. I. Anisimov, I. V. Solovyev, M. A. Korotin, M. T. Czyzyk and G. A. Sawatzky, Density-functional theory and NiO photoemission spectra, *Phys. Rev. B: Condens. Matter Mater. Phys.*, 1993, **48**, 16929.

47 M. Batzill and U. Diebold, The surface and materials science of tin oxide, *Prog. Surf. Sci.*, 2005, **79**, 47–154.

48 X. L. Wang, Z. Zeng and X. H. Zheng, First-principles investigations of Co- and Fe-doped SnO_2, *J. Appl. Phys.*, 2007, **101**, 09H104.

49 P. Novák, J. Kunes, L. Chaput and W. E. Pickett, Exact exchange for correlated electrons, *Phys. Status Solidi B*, 2006, **243**(3), 563–572.

50 M. T. Czyzyk and G. A. Sawatzky, Local-density functional and on-site correlations: The electronic structure of La_2CuO_4 and $LaCuO_3$, *Phys. Rev. B: Condens. Matter Mater. Phys.*, 1994, **49**, 14211.

51 T. Serin, N. Serin, S. Karadeniz, H. Sari, N. Tuğluoğlu and O. Pakma, Electrical, structural and optical properties of SnO_2 thin films prepared by spray pyrolysis, *J. Non-Cryst. Solids*, 2006, **352**, 209–215.

52 P. Saikia, A. Borthakur and P. K. Saikia, Structural, optical and electrical properties of tin oxide thin film deposited by APCVD method, *Indian J. Phys.*, 2011, **85**(4), 551–5589.

53 L. Yanlu, F. Weiliu, S. Honggang, C. Xiufeng, L. Pan, Z. Xian, H. Jingcheng and J. Minhua, Optical Properties of the High-Pressure Phases of SnO_2: First-Principles Calculation, *J. Phys. Chem. A*, 2010, **114**, 1052–1059.

54 A. Dar and A. Majid, *Eur. Phys. J.: Appl. Phys.*, 2015, **71**, 1.

55 X. Luo, X. Guo and Z. Liu, *Phys. Rev. B: Condens. Matter Mater. Phys.*, 2007, **76**, 9.

56 S. Saha, T. P. Sinha and A. Mookerjee, *Phys. Rev. B: Condens. Matter Mater. Phys.*, 2000, **62**, 13.

57 E. Klampaftis, D. Ross, K. R. McIntosh and B. S. Richards, Enhancing the performance of solar cells *via* luminescent down-shifting of the incident spectrum: A review, *Sol. Energy Mater. Sol. Cells*, 2009, **93**, 1182–1194.

58 F. Auzel, Upconversion and anti-Stokes processes with f and d ions in solids, *Chem. Rev.*, 2004, **104**, 139–174.

59 A. F. Lamrani, Rare-earth-doped TiO_2 rutile as a promising ferromagnetic alloy for visible light absorption in solar cells: first principle insights, *RSC Adv.*, 2020, **10**, 35505.

60 R. T. Wegh, H. Donker, K. D. Oskam and A. Meijerink, Visible quantum cutting in $LiGdF_4$: Eu^{3+} through downconversion, *Science*, 1999, **283**, 663–666.

61 F. J. DiSalvo, *Science*, 1999, **285**, 703–706.

62 J. R. Sootsman, D. Y. Chung and M. G. Kanatzidis, *Angew. Chem., Int. Ed.*, 2009, **48**, 8616–8639.